OPEN ACCESS
IOP Publishing
Measurement Science and Technology
Meas. Sci. Technol. **33** (2022) 035402 (10pp)
https://doi.org/10.1088/1361-6501/ac407a

Compressive nano-FTIR chemical mapping

Gerd Wübbeler[1,*], Manuel Marschall[1], Eckart Rühl[2], Bernd Kästner[1] and Clemens Elster[1]

[1] Physikalisch-Technische Bundesanstalt, Braunschweig and Berlin, Germany
[2] Physikalische Chemie, Freie Universität Berlin, Arnimallee 22, 14195 Berlin, Germany

E-mail: gerd.wuebbeler@ptb.de

Received 20 July 2021, revised 29 October 2021
Accepted for publication 6 December 2021
Published 24 December 2021

Abstract

Nano-Fourier-transform infrared spectroscopy (nano-FTIR) combines infrared spectroscopy with scanning probe microscopy (SPM) techniques and enables spectroscopic imaging of molecular and electronic properties of matter at nanometer spatial resolution. The spectroscopic imaging can be used to derive chemical mappings, i.e. the spatial distribution of concentrations of the species contained in a given sample. However, due to the sequential scanning principle underlying SPM, recording the complete spectrum over a large spatial area leads to long measurement times. Furthermore, the acquired spectrum often contains additional signals from species and lineshape effects that are not explicitly accounted for. A compressive chemical mapping approach is proposed for undersampled nano-FTIR data that utilizes sparsity of these additional signals in the spectral domain. The approach combines a projection technique with standard compressed sensing, followed by a spatially regularized regression. Using real nano-FTIR measurements superimposed by simulated interferograms representing the chemical mapping of the contained species, it is demonstrated that the proposed procedure performs well even in cases in which the simulated interferograms and the sparse additional signals exhibit a strong spectral overlap.

Keywords: nano-FTIR, compressed sensing, chemical mapping

(Some figures may appear in colour only in the online journal)

1. Introduction

Photons in the mid-infrared (IR) energyrange between 400 and 4000 cm^{-1}, corresponding to wavelengths between 2.5 and 25 μm, can induce a large number of light/matter interactions. These interactions can be exploited to gain specific information on the chemical composition and spatial distribution of the species contained in the sample [1]. In addition to vibrational properties, radiation in this energy regime reveals electronic [2] and quantum properties [3, 4]. Therefore, mid-IR spectroscopic methods are widely used in different fields including physics, material science, chemistry, biology, and medicine [1, 5–9]. However, the achievable spatial resolution of these optical techniques is limited by diffraction to about one half of the wavelength [10]. This restricts IR spectral imaging to a lateral resolution of several microns, which is often insufficient for accessing electrical, chemical, and thermal material properties of functional nanomaterials. Furthermore, due to the limited spatial resolution it is not possible to derive an understanding of the interactions between molecular species and biological matter.

To circumvent the diffraction limit when performing vibrational spectroscopy, advanced scanning probe microscopy (SPM) techniques have been developed in which SPM is combined with IR spectroscopy such as IR scanning near-field

* Author to whom any correspondence should be addressed.

optical microscopy (SNOM) and the photothermal induced resonance technique [11]. These techniques enable to record hyperspectral images (i.e. full IR spectra at each pixel) which can be used for structural or chemical analysis [12–18]. However, recording the complete spectrum at nanometer spatial resolution over an appreciable sample size is extremely inefficient, since data acquisition in SPM takes place in a sequential manner. Parallel detection schemes, as known from far-field spectroscopic imaging, do not exist. Furthermore, the still limited availability of intense broadband IR sources and the weakness of near-field signal intensities to be detected mean that a hyperspectral image can take hours to achieve a meaningful detection sensitivity (see, e.g. [14]). However, long measurement times can lead to sample and tip damage as well as to drift artifacts. This compromise between sensitivity and measurement time inhibits unfolding the potential of hyperspectral imaging for reliably differentiating and identifying chemical components (see, e.g. [19]).

Recently, it has been demonstrated that IR-SNOM measurements can be speed up significantly by means of compressed sensing techniques [15]. Compressed sensing is a signal processing technique that enables the complete reconstruction of a continuous signal based on a small number of measurements. Application of compressed sensing requires that the signal has a sparse representation with respect to some basis [20–23]. It turns out that many natural signals or images have such a sparse representation. Typical examples of employed basis functions include Fourier or wavelet bases; data-driven sparse dictionary learning methods have also been successfully employed [24]. Compressed sensing techniques have meanwhile been applied and even commercialized in different fields of physics, chemistry, and engineering (see [25] for a recent review). In IR spectroscopy, compressed sensing demonstrations exist for multidimensional spectroscopy [26], as well as for conventional far-field spectroscopy [27, 28]. A compressed FTIR approach utilizing a low-rank approximation has been presented in [29], a compressive method applying a rotating-frame transformation in [30], and an adaptive smart sampling approach combined with matrix completion techniques in [31].

In this work, a compressed sensing nano-Fourier-transform infrared spectroscopy (nano-FTIR) approach is developed that enables us to determine spatially resolved weights of species of interest given their known spectral characteristics. The approach accounts for signal contributions due the species with known spectral characteristics, as well as for additional signal contributions caused, e.g. by coupling of different excitations or simply by unknown species. Accounting for such additional signal contributions is necessary to achieve an accurate chemical mapping for the species of interest (see, e.g. [14]). Within the proposed compressed sensing approach, this additional signal contribution is assumed to have a sparse representation in the spectral domain. In order to determine the chemical mappings for the species of interest, a *joint regression and compressed sensing* approach is developed that takes randomly subsampled nano-FTIR data as input as well as a set of known interferograms. The capabilities of the proposed approach are demonstrated in a proof-of-principle study using a nano-FTIR data set [15] superimposed by simulated interferograms representing the chemical mapping of the species contained in a sample.

Note that the approach proposed in this work differs from the compressed sensing technique applied to nano-FTIR developed in [15]. While in [15] the reconstruction of nano-FTIR by compressed sensing techniques was demonstrated, the approach in this work aims at directly determining chemical mappings for species with *known* spectral properties from undersampled data. Furthermore, additional signal contributions are present which can be assumed to be sparse in the spectral domain. Note that the known spectra of the species of interest are not required to be sparse. As a consequence, corresponding nano-FTIR data following the superposition model introduced in section 3 could generally not be treated by compressed sensing techniques such as that used in [15].

2. Nano-FTIR

Nano-FTIR is based on scattering-type Fourier-transform IR spectroscopy combined with an atomic force microscope. Figure 1(a) shows a schematic diagram of the experimental setup. The incident IR radiation is backscattered from a metallic tip that scans the sample surface. The metallic tip acts as an optical antenna which strongly confines the incident optical field around the tip apex, resulting in a nanoscale light source suitable for high-resolution imaging and spectroscopy. The backscattered light is analyzed by means of a Michelson interferometer and the interferogram is recorded as a function of the optical path difference [32, 33]. The corresponding near-field spectrum can be obtained from a Fourier-transform of the interferogram.

In this work, nano-FTIR data recorded at the metrology light source electron storage ring [34] are utilized. The data were obtained from a graphene-coated silicon carbide surface modified by a mechanical indent. For a detailed description of the experimental setup and sample preparation, we refer to [15]. Altogether, 1804 interferograms were recorded on a rectangular area of 60 μm^2 using a Cartesian grid with 41×44 spatial locations. Each complex-valued interferogram was sampled at 1024 equidistant optical path differences using a step size of 1.56 μm. The resulting spectral resolution is 6.26 cm^{-1}. The full nano-FTIR data set can thus be represented by a 3D data cube with dimensions of $41 \times 44 \times 1024$. Figures 1(b) and (d) show the interferogram and the corresponding Fourier magnitude spectrum determined at the center pixel. As can be seen, the spectrum is dominated by a narrow peak at about 900 cm^{-1}. Similar spectra are observed at all spatial locations, indicating the spectral sparseness of this data set due to the phonon polariton resonance [35]. However, the spectral peaks also exhibit some variation regarding their magnitude and shape, as illustrated in figure 1(c), which shows the spatial distribution of this spectral feature.

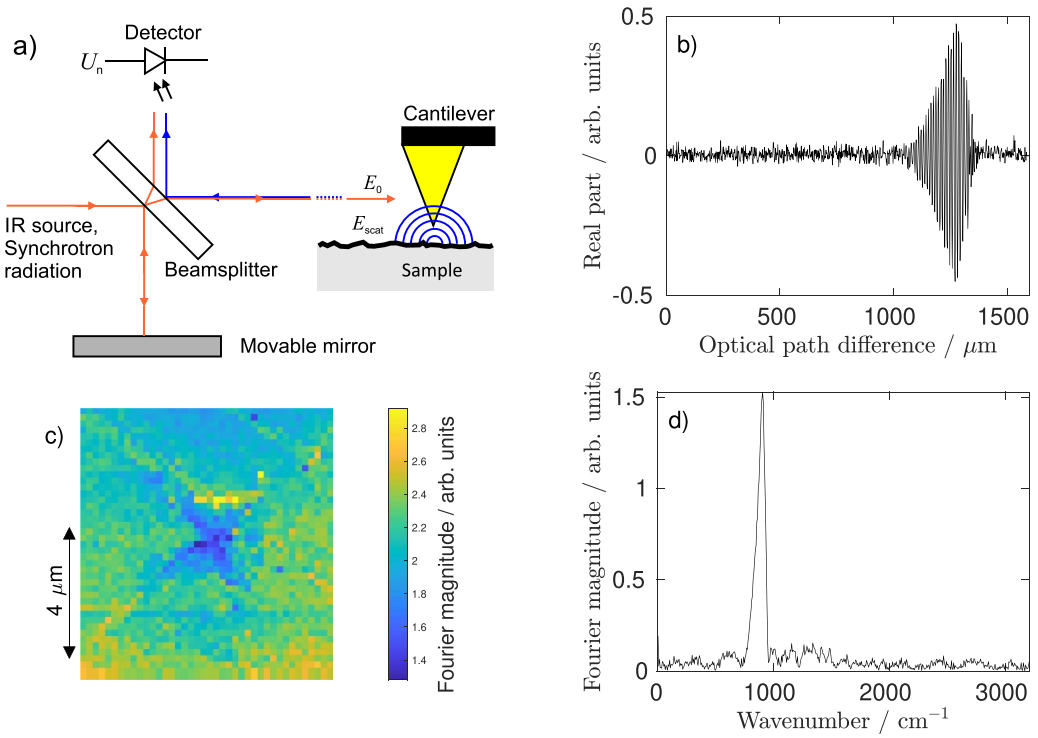

Figure 1. Schematic plot of the experimental setup (a) and plots of nano-FTIR data obtained from a graphene-coated silicon carbide surface ((b) to (d)). (b) Shows the real part of the interferogram taken at the center of the sample area, and (d) shows the corresponding magnitude spectrum of its Fourier transform. In (c), the spatial distribution of the peak spectral magnitude at about 900 cm^{-1} is depicted. The surface size shown in (c) is 7.5 µm × 8.0 µm = 60 µm^2.

3. Compressive chemical mapping

A joined regression and compressed sensing approach is developed that enables a chemical mapping for species of interest given their known spectral characteristics. The interferogram $y(l)$ taken at a single spatial location as a function of the optical path difference l (cf figure 1(a)) is modeled as

$$y(l) = \theta_1 X_1(l) + \theta_2 X_2(l) + \cdots \theta_p X_p(l) + S(l)\,, \qquad (1)$$

where $\theta_1, \theta_2, \ldots, \theta_p$ represent the sought weights, and where the known interferograms $X_1(l), X_2(l), \ldots, X_p(l)$ may also include contributions from the substrate material. Determining the weights $\theta_1, \theta_2, \ldots, \theta_p$ at different spatial locations enables a chemical mapping in terms of the spatial weight distributions of the species of interest. The term $S(l)$ in equation (1) models the additional signal contributions to the recorded interferogram $y(l)$, and $S(l)$ is assumed to have a sparse representation in the spectral domain. The model expressed by equation (1) represents a joint regression and compressed sensing task for which a two step procedure is developed that takes randomly subsampled nano-FTIR data as input as well as a set of known interferograms $X_1(l), X_2(l), \ldots, X_p(l)$.

In section 3.1, a projection technique is applied leading to a standard compressed sensing task whose solution provides the sparse representation of the additional signal $S(l)$. Section 3.2 then describes, how this sparse representation is combined with the set of known interferograms $X_1(l), X_2(l), \ldots, X_p(l)$, leading to a linear system of equations. The solution of this linear system, which also includes a regularization that favors spatial smoothness, then yields an estimate of the spatial distribution of the weights $\theta_1, \theta_2, \ldots, \theta_p$ of the species of interest.

3.1. Evaluation of the sparse signal

The approach described in this work utilizes compressed sensing techniques [20–23]. These techniques allow a continuous signal to be reconstructed based on a small number of randomly selected measurements, provided that the sought signal is sparse with respect to some basis. Here, we assume that the additional signal contribution (denoted as $S(l)$ in equation (1)) has a sparse representation in the spectral domain so that compressed sensing techniques can be applied for that part of the signal. Each measured interferogram is considered as the sum of a sparse signal and a signal due to different species with known interferograms. A subsampled interferogram taken at a single spatial location is modeled as

$$y = X\theta + V\mu\,, \qquad (2)$$

where y denotes an $n \times 1$ vector of interferogram values, with n being the number of randomly selected optical path differences. The term $X\theta$ models the signal of p contained species. The columns of the known $n \times p$ matrix X are obtained from the corresponding interferograms $X_1(l), X_2(l), \ldots, X_p(l)$, which are evaluated at the selected optical path differences.

The $p \times 1$ vector θ summarizes the corresponding weights $\theta_1, \theta_2, \ldots, \theta_p$ of these signals. The term $V\mu$ in equation (2) models the sparse signal $S(l)$ at the selected optical path differences. The $n \times m$ matrix V is constructed from the rows of the $m \times m$ discrete Fourier matrix corresponding to the selected optical path differences. The dimension m with $m \gg n$ denotes the number of optical path differences of a fully sampled interferogram. The $m \times 1$ vector μ encodes the sparse representation; this implies that μ has only a few non-zero elements, p_0, where $p_0 \ll n$. The goal of the analysis is to determine the weights $\theta_1, \theta_2, \ldots, \theta_p$ of the interferograms of the contained species.

Solving equation (2) for θ and μ can be viewed as a joint regression and compressed sensing task for which, however, no standard methods are available. In order to make compressed sensing techniques applicable, equation (2) is multiplied (from the left) by an $(n-p) \times n$ matrix P which satisfies $PX = 0$. The choice of the matrix P is described in appendix A. Application of the matrix P then leads to the linear model

$$\tilde{y} = PV\mu \tag{3}$$

with $\tilde{y} = Py$, where the contribution due to the known interferograms of the contained species has been removed. The construction of the matrix P and mathematical details are presented in appendix A.

The linear model expressed by equation (3) can be treated as a standard compressed sensing task leading to the following optimization problem

$$\min_{\mu} \|\mu\|_0 \quad \text{subject to} \quad \tilde{y} = PV\mu\,, \tag{4}$$

where $\|\mu\|_0$ denotes the number of nonzero elements of the vector μ.

While a direct solution of equation (4) is usually computationally not feasible, the compressed sensing task can often be simplified by replacing the l_0-norm with the l_1 norm; this leads to a convex optimization problem [36, 37]. Alternatively, so-called 'greedy methods' can be applied that allow one to determine an approximate solution in short time (see, e.g. [20]). To this end, we have utilized the orthogonal matching pursuit algorithm [38]. The resulting vector μ then provides a sparse representation of the additional signal $S(l)$ in terms of the relevant Fourier basis functions indicated by the non-zero elements of μ.

3.2. Chemical mapping using spatial regression

Once the method described above has been applied individually to each recorded interferogram, the resulting set of vectors μ obtained from all spatial locations is summarized by determining the Fourier basis functions most frequently encountered in all subsampled interferograms. Under the assumption that the additional sparse signal is a superposition of the same subset of basis functions at all spatial locations, this subset is inferred as the p_0 basis functions that appear most often in the compressed sensing solutions at the different spatial locations. The number p_0 of relevant basis functions chosen is a compromise between a small p_0 and a suitable representation of the sparse signal at all spatial locations. Note that, while the subset of basis functions is fixed in this way, their corresponding weights can still vary spatially.

The selected subset of basis functions is then combined with the known interferograms $X_1(l), X_2(l), \ldots, X_p(l)$ of the contained species in order to define a linear system of equations that allows all measured interferograms recorded at different spatial locations to be modeled simultaneously. The sought weights $\theta_1, \theta_2, \ldots, \theta_p$ of the interferograms as well as the weights of the selected subset of Fourier basis functions vary spatially and could be estimated at each spatial location individually. However, this spatial variation can be assumed to be smooth which is exploited by fitting all weights jointly after including an additional regularization functional that favors their spatial smoothness. The regularization functional is based on an intrinsic Gaussian Markov random field [39] and is specified in appendix B. The strength of the smoothness regularization is determined by applying an L-curve criterion [40].

4. Results

4.1. Nano-FTIR regression data

In order to assess the effectiveness of the proposed compressive chemical mapping approach, the 3D nano-FTIR data set communicated in [15] was augmented by simulated regression components representing hypothetical contained species. In this way, the nano-FTIR measurements are used here to represent a realistic signal that is sparse in the spectral domain and includes realistic experimental noise (cf figure 1(b)). For the regression components, three simulated magnitude spectra labeled A, B, and C were generated; these spectra are depicted in figure 2(a) with their corresponding interferograms (figure 2(b)). As can be seen, the three spectra A, B, and C exhibit different spectral overlap with respect to the sparse spectrum, where A has the strongest spectral overlap. Figures 2(c)–(e) show the spatial mappings of the weights associated with each of these three interferograms.

An augmented 3D nano-FTIR data set was generated by adding the interferograms, weighted by the local weights according to their spatial mappings, to the nano-FTIR measurement data. To test the proposed method for compressive chemical mapping, a simulated test scenario was constructed by considering only a subset of the whole data set. The subset was formed by randomly selecting 20% of the samples from the augmented data set. The random samples were selected uniformly along the interferometer axis and within the image plane. Before applying the proposed compressive chemical mapping procedure, complex-valued Gaussian white noise with a signal-to-noise ratio of 500 was added to the interferograms A, B, and C. This was done because, for real data, these interferograms are expected to be determined by separate measurements, e.g. by recording the interferograms using reference spectra of pure substances. During the analysis, a fixed

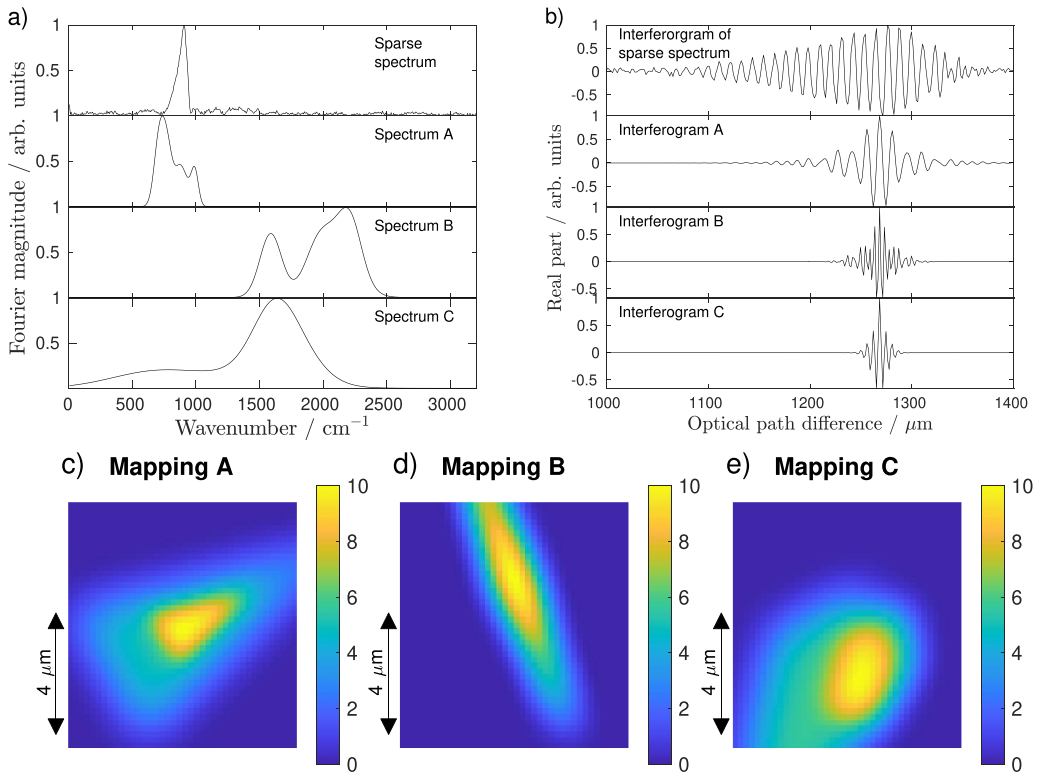

Figure 2. Simulated regression components used for the assessment of the proposed approach. (a) Shows the simulated magnitude spectra A, B, and C as well as the (normalized) sparse spectrum at the center pixel. In (b), the real parts of the corresponding interferograms are depicted. (c), (d), and (e) Show the simulated spatial mappings of the three regression components (with the same surface size as in figure 1(c)).

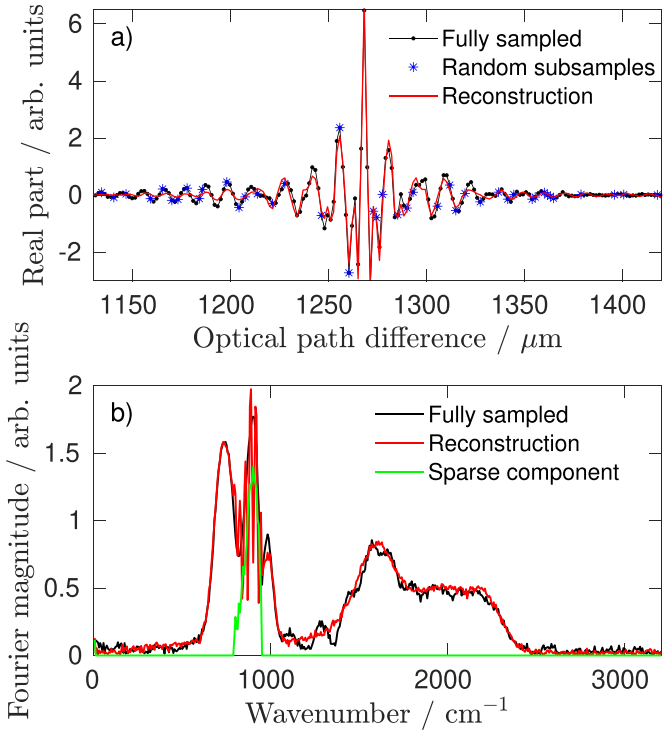

Figure 3. Reconstruction results obtained from the proposed compressive chemical mapping approach. (a) Shows the fully sampled interferogram at the center pixel (black dots) together with the randomly subsampled data (20%) (blue stars) and the resulting reconstruction (red line). (b) Shows the magnitude spectra corresponding to the fully sampled (black line) and reconstructed interferogram (red line) as well as the reconstructed sparse spectral component (green line).

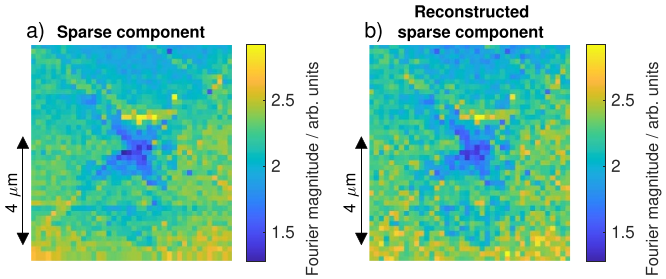

Figure 4. Comparison of the spatial patterns of the Fourier magnitude at about 900 cm^{-1}. (a) Fourier magnitude of the original experimental data (same as figure 1(c)). (b) Fourier magnitude of the reconstructed sparse signal determined from the augmented and randomly subsampled data (same surface size as figure 1(c)).

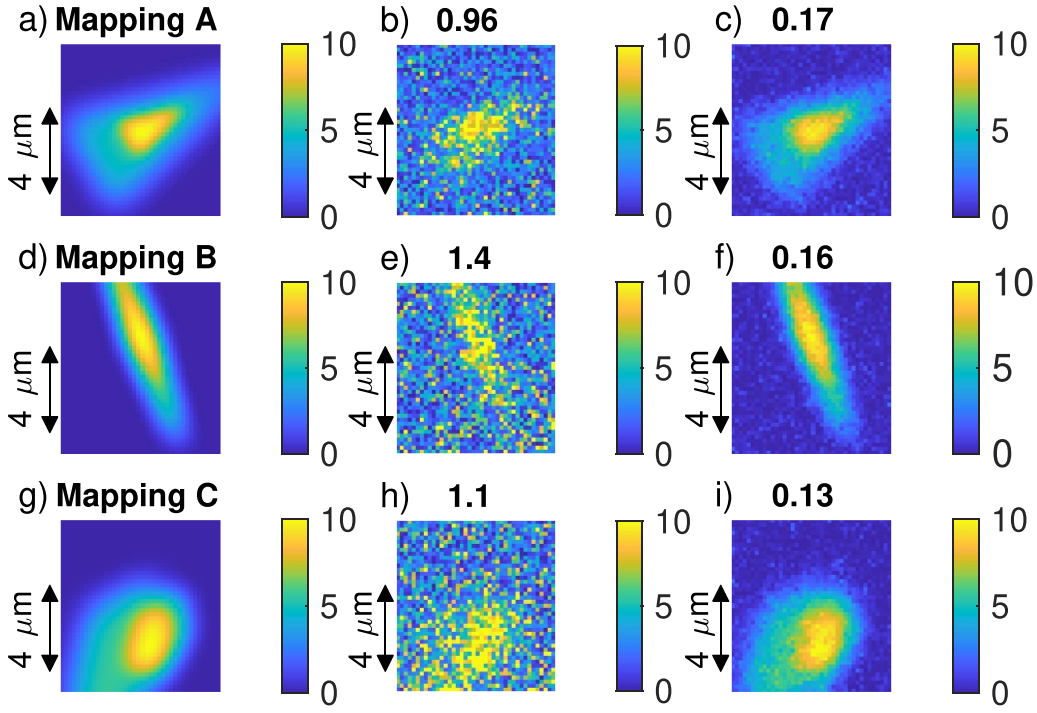

Figure 5. Chemical mapping results obtained from a subsampling rate of 20% (same surface size as figure 1(c). The left column ((a), (d), and (g)) shows the true mappings of the components A, B and C, and the right column ((c), (f), and (i)) the resulting mappings obtained from the proposed compressive chemical mapping approach. The center column ((b), (e), and (h)) shows the corresponding results from the simple regression approach, which does not account for the sparse signals. The number above each plot indicates the relative error.

value of $p_0 = 50$ was taken for the number of relevant Fourier basis functions representing the sparse signal.

In addition to the proposed procedure, we also applied a simple regression analysis to the same data; this analysis uses the interferograms of the components A, B, and C only, ignoring the presence of the sparse signal. Thus, the sparse signal is treated as an (additional) source of error within this simple regression approach. In order to enable a realistic comparison of both methods, the simple regression approach also includes a spatial smoothness regularization carried out in the same way as for the proposed approach.

4.2. Reconstruction and chemical mapping

The proposed procedure enables a reconstruction of the full 3D nano-FTIR data from randomly subsampled data. In figure 3, the results obtained from the center pixel are shown. As can be seen, the approach yields a reliable reconstruction of the interferogram as well as of the corresponding magnitude spectrum. The reconstruction also includes a decomposition of the data into the regression components and the sparse signal. This is demonstrated in figure 4 showing a high agreement between the resulting spatial pattern of the Fourier magnitude of the sparse signal (taken at 900 cm^{-1}) and the corresponding pattern determined for the original experimental data.

The results obtained from the chemical mappings of components A, B, and C when using a subsampling rate of 20% are depicted in figure 5. Figures 5(a), (d), and (g) show the true mappings of these components, while (c), (f), and (i) show the resulting mappings obtained from the proposed compressive chemical mapping approach. Figures 5(b), (e), and (h) show corresponding results by the simple regression approach

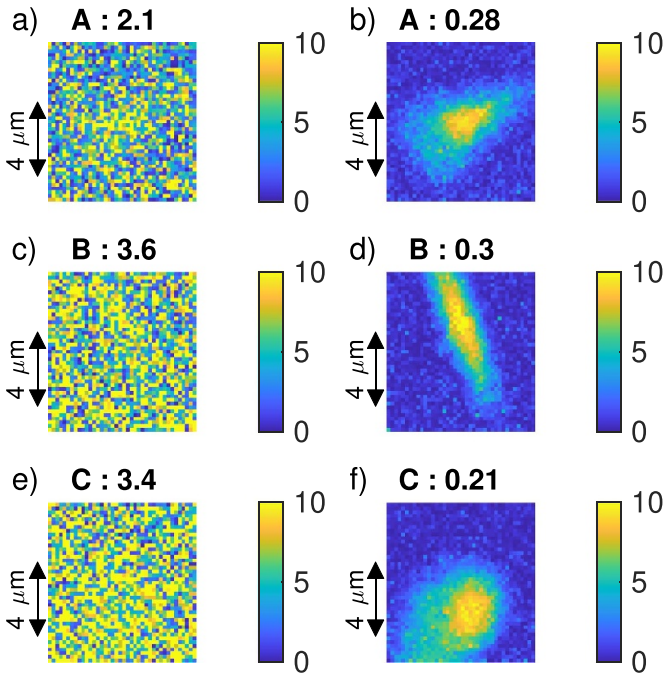

Figure 6. Chemical mapping results for the three components A, B, and C obtained from a subsampling rate of 10% (same surface size as figure 1(c)). The right column ((b), (d), and (f)) shows the results obtained from the proposed compressive chemical mapping approach and the left column ((a), (c), and (e)) those obtained from the simple regression approach. The number above each plot indicates the relative error.

Table 1. Relative errors resulting for the proposed chemical mapping approach for the components A, B, and C in dependence on the subsampling rate.

Subsampling rate/%	50	30	20	15	10	7.5	5
Mapping A	0.14	0.16	0.17	0.20	0.28	0.49	1.58
Mapping B	0.11	0.15	0.16	0.20	0.30	0.56	1.98
Mapping C	0.09	0.13	0.13	0.15	0.21	0.41	1.36

which does not account for the sparse signals. As can be seen, the mappings obtained from the proposed method show a high agreement with the true mappings, whereas the original patterns are barely visible when using the simple regression approach. This is also demonstrated in terms of relative errors indicated above the resulting mappings in figure 5. The relative errors have been calculated as $\|\hat{\theta} - \theta\|_F / \|\theta\|_F$, where $\|\cdot\|_F$ denotes the Frobenius norm, and where $\hat{\theta}$ and θ denote the estimated and the true chemical mapping, respectively.

We also applied the proposed method to the augmented nano-FTIR data set when a subsampling rate of only 10% is used. The corresponding results are shown in figures 6(b), (d), and (f). As expected, reducing the amount of data entails some deterioration of the chemical mappings, which also exhibit more noise when compared to the results obtained from 20% subsampling shown in figure 5. This is also indicated by the increased levels of relative errors. Nevertheless, the main features of the true patterns are still clearly visible when applying the proposed approach. In contrast, application of the simple regression approach does not yield a reasonable result if a subsampling rate of 10% is used.

In table 1, the relative errors resulting for proposed chemical mapping approach for the augmented nano-FTIR data in dependence on the subsampling rate are listed. As expected, small relative errors are observed for large values of the subsampling rate whereas for subsampling rates below 10% the relative errors exhibit a marked increase. In addition, despite their distinctly different spectral properties (cf figures 2(a) and (b)), roughly the same error rates are observed for the components A, B, and C for a given subsampling rate. Note that the usability of small subsampling rates may also depend on different aspects such as the sparsity of the sparse signal, the SNR, the number of the sought chemical mappings, their line profiles as well as their spatial resolution. A detailed analysis of the impact of these effects is referred to future work.

5. Conclusions

Nano-FTIR spectroscopy allows for molecular imaging at nanometer-scale resolution which can be used to derive a

chemical mapping in terms of the spatial distribution of concentrations of the contained species. However, the inherent sequential scanning principle severely limits its application due to long acquisition times. In order to accelerate nano-FTIR spectroscopy, compressed sensing techniques can be applied that require only a small number of randomly selected samples and utilize a sparsity assumption for data reconstruction. The joint regression and compressed sensing nano-FTIR approach developed in this work enables the chemical mapping of species for which interferograms are available. The approach also accounts for additional signal contributions whose IR spectra are assumed to be sparse. The capabilities of the proposed approach are demonstrated in terms of real nano-FTIR measurement data augmented by simulated interferograms. It is shown that the presented approach allows for a reliable determination of the chemical mappings even when their corresponding IR spectra exhibit a strong spectral overlap and blend with the sparse signal. The approach also enables a decomposition of the data into the individual components and the sparse signal. Future work could address the development of a Bayesian inference procedure that treats the estimation of the different components and the sparse signal simultaneously in a coherent way, and which lends itself naturally to an uncertainty quantification of the results.

Data availability statement

The data that support the findings of this study are available upon reasonable request from the authors.

Acknowledgment

Financial support from the Deutsche Forschungsgemeinschaft DFG (Grants EL 492/1-1, RU 420/13-1) of this work is gratefully acknowledged.

Appendix A. Construction of the matrix *P*

Let $v_1,\ldots,v_m$ denote a complex valued orthonormal basis in $\mathbb{C}^m$. Denote as V the $n\times m$ matrix with entries $V_{ij}=(v_j)_i$, where $j=1,\ldots,m$, $i\in\{i_1,\ldots,i_n\}$ with $n<m$. Consider the model

$$y = X\theta + V\mu\,, \tag{A.1}$$

where X denotes a complex-valued $n\times p$ design matrix assumed to have rank p, i.e. the columns of X are assumed to be linearly independent. The $m\times 1$ complex-valued vector μ is sparse, with only r components being different from zero. Let $\tilde{\mu}=(\mu_{i1},\ldots,\mu_{ir})^T$ denote the vector of the non-zero components of μ, and $\widetilde{V}=(v_{i1},\ldots,v_{ir})$ the $n\times r$ matrix with corresponding columns of V. The subscript T indicates 'transpose'.

The goal is to reconstruct the complex-valued θ (and perhaps $\tilde{\mu}$) given y, X, V and the sparsity assumption about μ. A necessary condition for the problem to be well-posed (i.e. for θ being identifiable) is that

$$\operatorname{rank}([X,\widetilde{V}]) = p+r\,. \tag{A.2}$$

Application of a QR-decomposition [41] to the matrix X yields

$$X = QR\,, \tag{A.3}$$

where the $n\times n$ matrix Q is unitary, i.e. it satisfies $Q^HQ=I$, and where the $n\times p$ matrix R is upper triangular. The subscript H indicates the conjugate transpose (or Hermitian transpose). Denoting the columns of the $n\times n$ matrix Q as $q_1,q_2,\ldots,q_n$, the $(n-p)\times n$ matrix $P=(q_{p+1},\cdots,q_n)^H$ is chosen which satisfies $PX=0$. Note that the condition $PX=0$ does not define the matrix P uniquely. The specific choice made here can be recommended when assuming the data to be affected by homoscedastic independent Gaussian random errors. Application of the matrix P to (A.1) leads to

$$\tilde{y} = PV\mu\,, \tag{A.4}$$

which constitutes an ordinary analysis task of compressed sensing in terms of the transformed signal $\tilde{y}$ with dimension $(n-p)\times 1$ and the basis set given by the $(n-p)\times m$ matrix PV. Due to the above-stated rank condition, (A.4) leaves the non-zero components of μ identifiable, and because of (A.2), subsequent identification of θ is possible.

Appendix B. Spatial regression and regularization

The selected subset of Fourier basis functions and the known interferograms are fitted to the data at all spatial locations simultaneously by minimizing

$$\sum_{\vec{r}} \|y_{\vec{r}} - X_{\vec{r}}\theta_{\vec{r}} - \widetilde{V}_{\vec{r}}\tilde{\mu}_{\vec{r}}\|^2 + \lambda\left(\sum_{i=1}^{p}(\theta^{(i)})^H S\theta^{(i)} + \sum_{i=1}^{r}(\tilde{\mu}^{(i)})^H S\tilde{\mu}^{(i)}\right), \tag{B.1}$$

where $y_{\vec{r}}$ denotes the $n_{\vec{r}}\times 1$ vector of interferogram values at spatial position $\vec{r}$, $X_{\vec{r}}$ the $n_{\vec{r}}\times p$ corresponding design matrix for the known interferograms, $\widetilde{V}_{\vec{r}}$ the $n_{\vec{r}}\times r$ design matrix for the selected subset of basis functions at spatial position $\vec{r}$, and the $r\times 1$ vector $\tilde{\mu}_{\vec{r}}$ the corresponding coefficients.

The λ-term in (B.1) represents a regularization favoring spatial smoothness. The vector $\theta^{(i)}$ contains the ith component of θ at all spatial positions and similarly $\tilde{\mu}^{(i)}$. The structure matrix S with dimension $n_{\vec{r}}\times n_{\vec{r}}$ is given by

$$S_{ij} = \begin{cases} -1, & i\sim j \\ n_i, & i=j \\ 0, & \text{otherwise} \end{cases}\,. \tag{B.2}$$

where $i\sim j$ indicates that positions i and j are neighboring positions. We use a configuration with eight neighbors assigned for interior pixels. The relationship to a Gaussian Markov random field is that S is often utilized as a precision matrix in an intrinsic Gaussian Markov random field [39]. Because S

does not have full rank, the corresponding Gaussian random field is improper. A regularization using the structure matrix S favors similar values for the coefficients of neighboring pixels. The parameter λ specifies the strength of the smoothness regularization and is determined by an L-curve criterion [40]. For the chemical mapping results presented in this work, the magnitude of the resulting complex-valued weights θ was taken.

ORCID iDs

Gerd Wübbeler https://orcid.org/0000-0002-6871-8903
Manuel Marschall https://orcid.org/0000-0003-0648-1936

References

[1] Salzer R and Siesler H W 2014 *Infrared and Raman Spectroscopic Imaging* (Weinheim: Wiley)
[2] Lau W S 1999 *Infrared Characterization for Microelectronics* (Singapore: World Scientific Publishing)
[3] Zayats A and Richards D (eds) 2009 *Nano-Optics and Near-Field Optical Microscopy* (Boston, MA: Artech House)
[4] Kuzmany H 2009 *Solid-State Spectroscopy* (Berlin: Springer)
[5] Helm D, Labischinski H, Schallehn G and Naumann D 1991 Classification and identification of bacteria by Fourier-transform infrared spectroscopy *Microbiology* **137** 69–79
[6] Downey G 1998 Food and food ingredient authentication by mid-infrared spectroscopy and chemometrics *TRAC Trends Anal. Chem.* **17** 418–24
[7] Fernandez D C, Bhargava R, Hewitt S M and Levin I W 2005 Infrared spectroscopic imaging for histopathologic recognition *Nat. Biotechnol.* **23** 469–74
[8] Mohsin G F, Schmitt F-J, Kanzler C, Epping J D, Flemig S and Hornemann A 2018 Structural characterization of melanoidin formed from d-glucose and l-alanine at different temperatures applying FTIR, NMR, EPR and MALDI-ToF-MS *Food Chem.* **245** 761–7
[9] Hornemann A, Sinning D, Cortes S, Campino L, Emmer P, Kuhls K, Ulm G, Frohme M and Beckhoff B 2017 A pilot study on fingerprinting Leishmania species from the Old World using Fourier transform infrared spectroscopy *Anal. Bioanal. Chem.* **409** 6907–23
[10] Born M and Wolf E 1999 *Principles of Optics: Electromagnetic Theory of Propagation, Interference and Diffraction of Light* (Cambridge: Cambridge University Press)
[11] Muller E A, Pollard B and Raschke M B 2015 Infrared chemical nano-imaging: accessing structure, coupling and dynamics on molecular length scales *J. Phys. Chem. Lett.* **6** 1275–84
[12] Amarie S, Zaslansky P, Kajihara Y, Griesshaber E, Schmahl W W and Keilmann F 2012 Nano-FTIR chemical mapping of minerals in biological materials *Beilstein J. Nanotechnol.* **3** 312–23
[13] Huth F, Govyadinov A, Amarie S, Nuansing W, Keilmann F and Hillenbrand R 2012 Nano-FTIR absorption spectroscopy of molecular fingerprints at 20 nm spatial resolution *Nano Lett.* **12** 3973–8
[14] Amenabar I, Poly S, Goikoetxea M, Nuansing W, Lasch P and Hillenbrand R 2017 Hyperspectral infrared nanoimaging of organic samples based on Fourier transform infrared nanospectroscopy *Nat. Commun.* **8** 1–10
[15] Kästner B *et al* 2018 Compressed sensing FTIR nano-spectroscopy and nano-imaging *Opt. Express* **26** 18115
[16] Hao Z, Bechtel H A, Kneafsey T, Gilbert B and Nico P S 2018 Cross-scale molecular analysis of chemical heterogeneity in shale rocks *Sci. Rep.* **8** 1–9
[17] Szostak R, Silva J, Turren-Cruz S-H, Soares M, Freitas R, Hagfeldt A, Tolentino H and Nogueira A 2019 Nanoscale mapping of chemical composition in organic-inorganic hybrid perovskite films *Sci. Adv.* **5** eaaw6619
[18] Kurouski D, Dazzi A, Zenobi R and Centrone A 2020 Infrared and Raman chemical imaging and spectroscopy at the nanoscale *Chem. Soc. Rev.* **49** 3315–47
[19] Lasch P, Haensch W, Naumann D and Diem M 2004 Imaging of colorectal adenocarcinoma using FT-IR microspectroscopy and cluster analysis *Biochim. Biophys. Acta Mol. Basis Dis.* **1688** 176–86
[20] Eldar Y C and Kutyniok G 2012 *Compressed Sensing: Theory and Applications* (Cambridge: Cambridge University Press)
[21] Donoho D L 2006 Compressed sensing *IEEE Trans. Inf. Theory* **52** 1289–306
[22] Candes E J, Romberg J K and Tao T 2006 Stable signal recovery from incomplete and inaccurate measurements *Commun. Pure Appl. Math.* A **59** 1207–23
[23] Candes E J and Tao T 2006 Near-optimal signal recovery from random projections: universal encoding strategies? *IEEE Trans. Inf. Theory* **52** 5406–25
[24] Kreutz-Delgado K, Murray J F, Rao B D, Engan K, Lee T-W and Sejnowski T J 2003 Dictionary learning algorithms for sparse representation *Neural Comput.* **15** 349–96
[25] Gamez G 2016 Compressed sensing in spectroscopy for chemical analysis *J. Anal. At. Spectrom.* **31** 2165–74
[26] Dunbar J A, Osborne D G, Anna J M and Kubarych K J 2013 Accelerated 2D-IR using compressed sensing *J. Phys. Chem. Lett.* **4** 2489–92
[27] Katz O, Levitt J M and Silberberg Y 2010 Compressive fourier transform spectroscopy *Frontiers in Optics 2010/Laser Science XXVI, OSA Technical Digest (CD)* (Optical Society of America) p FTuE3
[28] Brady S P, Do M N and Bhargava R 2009 Reconstructing FT-IR spectroscopic imaging data with a sparse prior *2009 16th IEEE Int. Conf. on Image Processing (ICIP)* (IEEE) pp 829–32
[29] Marschall M, Hornemann A, Wübbeler G, Hoehl A, Rühl E, Kästner B and Elster C 2020 Compressed FTIR spectroscopy using low-rank matrix reconstruction *Opt. Express* **28** 38762–72
[30] Johnson S C, Muller E A, Khatib O, Bonnin E A, Gagnon A C and Raschke M B 2019 Infrared nanospectroscopic imaging in the rotating frame *Optica* **6** 424–9
[31] Labouesse S, Johnson S C, Bechtel H A, Raschke M B and Piestun R 2020 Smart scattering scanning near-field optical microscopy *ACS Photon.* **7** 3346–52
[32] Hermann P, Hoehl A, Patoka P, Huth F, Rühl E and Ulm G 2013 Near-field imaging and nano-Fourier-transform infrared spectroscopy using broadband synchrotron radiation *Opt. Express* **21** 2913–19
[33] Hermann P *et al* 2017 Enhancing the sensitivity of nano-FTIR spectroscopy *Opt. Express* **25** 16574–88
[34] Gottwald A, Klein R, Müller R, Richter M, Scholze F, Thornagel R and Ulm G 2012 Current capabilities at the metrology light source *Metrologia* **49** S146
[35] Huber A, Ziegler A, Köck T and Hillenbrand R 2009 Infrared nanoscopy of strained semiconductors *Nat. Nanotechnol.* **4** 153–7

[36] Cohen A, Dahmen W and DeVore R 2009 Compressed sensing and best k-term approximation *J. Am. Math. Soc.* **22** 211–31
[37] Chen S S, Donoho D L and Saunders M A 2001 Atomic decomposition by basis pursuit *SIAM Rev.* **43** 129–59
[38] Tropp J A and Gilbert A C 2007 Signal recovery from random measurements via orthogonal matching pursuit *IEEE Trans. Inf. Theory* **53** 4655–66
[39] Rue H and Held L 2005 *Gaussian Markov Random Fields: Theory and Applications* (New York: CRC Press)
[40] Hansen P C 1992 Analysis of discrete ill-posed problems by means of the L-curve *SIAM Rev.* **34** 561–80
[41] Golub G H and Van Loan C F 2013 *Matrix Computations* vol 3 (Baltimore: JHU Press)